ARTICLE

Heterogeneous FASnI₃ Absorber with Enhanced Electric Field for High-Performance Lead-Free Perovskite Solar Cells

Tianhao Wu[1,3], Xiao Liu[2] ✉, Xinhui Luo[1], Hiroshi Segawa[2], Guoqing Tong[3], Yiqiang Zhang[4], Luis K. Ono[3], Yabing Qi[3], Liyuan Han[1,2] ✉

HIGHLIGHTS

- A novel strategy to further improve the efficiency of lead-free tin perovskite solar cells by carefully controlling the built-in electric field in the absorber is described.

- A promising efficiency of 13.82% was obtained based on the formamidinium tin iodide (FASnI₃) perovskite solar cells with a vertical Sn^{2+} gradient and an enhanced electric field.

- The solar cell with a heterogeneous FASnI₃ absorber is ultrastable, maintaining over 13% efficiency after operation under 1-sun illumination for 1,000 h in air.

ABSTRACT Lead-free tin perovskite solar cells (PSCs) have undergone rapid development in recent years and are regarded as a promising eco-friendly photovoltaic technology. However, a strategy to suppress charge recombination via a built-in electric field inside a tin perovskite crystal is still lacking. In the present study, a formamidinium tin iodide (FASnI₃) perovskite absorber with a vertical Sn^{2+} gradient was fabricated using a Lewis base-assisted recrystallization method to enhance the built-in electric field and minimize the bulk recombination loss inside the tin perovskites. Depth-dependent X-ray photoelectron spectroscopy revealed that the Fermi level upshifts with an increase in Sn^{2+} content from the bottom to the top in this heterogeneous FASnI₃ film, which generates an additional electric field to prevent the trapping of photo-induced electrons and holes. Consequently, the Sn^{2+}-gradient FASnI₃ absorber exhibits a promising efficiency

of 13.82% for inverted tin PSCs with an open-circuit voltage increase of 130 mV, and the optimized cell maintains over 13% efficiency after continuous operation under 1-sun illumination for 1,000 h.
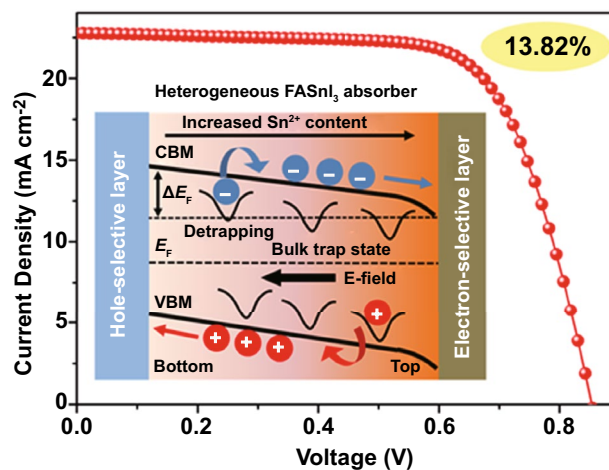
✉ Xiao Liu, liu.xiao@mail.u-tokyo.ac.jp; Liyuan Han, han.liyuan@sjtu.edu.cn

[1] State Key Laboratory of Metal Matrix Composites, School of Material Science and Engineering, Shanghai Jiao Tong University, Shanghai 200240, People's Republic of China

[2] Special Division of Environmental and Energy Science, Komaba Organization for Educational Excellence (KOMEX), College of Arts and Sciences, University of Tokyo, Tokyo 153-8902, Japan

[3] Energy Materials and Surface Sciences Unit (EMSSU), Okinawa Institute of Science and Technology Graduate University (OIST), 1919-1 Tancha, Onna-son, Kunigami-gun, Okinawa 904-0495, Japan

[4] School of Materials Science and Engineering, Henan Institute of Advanced Technology, Zhengzhou University, Zhengzhou 450001, People's Republic of China

1 Introduction

Lead-free tin halide perovskites with eco-friendly properties, high carrier mobility, and a suitable bandgap close to the Shockley–Queisser limit are regarded as promising candidates for developing next-generation perovskite solar cells (PSCs) [1–6]. In recent years, the power conversion efficiency (PCE) of tin PSCs based on the formamidinium tin iodide (FASnI$_3$) perovskite absorber has increased to over 10% [7–11]. One important reason for this rapid PCE growth is an increase in carrier diffusion length in the tin perovskite layer. This has been enabled by introducing large organic cations such as n-butylammonium (BA), phenylethylammonium (PEA), guanidinium (GA), and pentafluorophen-oxyethylammonium (FOE) to form a low-dimensional tin perovskite phase and produce a highly oriented polycrystalline film [12–17] or by introducing reducing agents to eliminate Sn^{4+} impurities, such as tin halides (SnX$_2$), metallic Sn, hydroxybenzene sulfonic acid, and formic acid [18–22]. Furthermore, the architecture of tin PSCs has evolved from a regular (n-i-p) to an inverted (p-i-n) structure to avoid oxidization of Sn^{2+} by the chemical dopants of hole transport materials used in the n-i-p structure, resulting in better device stability [23–25].

After the PCE reached 10%, many studies focused on the surface passivation of the tin perovskite layer to minimize the deficit between the bandgap and open-circuit voltage (V_{OC}) in tin PSCs [26–29]. For example, an edamine with a lone electron pair was applied to passivate the FASnI$_3$ perovskite surface via a coordination reaction with the unsaturated Sn^{2+}, resulting in 50% enhancement of the carrier lifetime and increased V_{OC} of tin PSCs by 100 mV to 0.6 V [30]. Similarly, gallic acid, hydroxybenzene sulfonic acid, and thiosemicarbazide molecules with coordination functional groups have also been applied as surface passivation agents for tin PSCs to increase the photovoltage [21, 26, 31]. Additionally, a p-type semiconducting polymer with amine groups was used to passivate the bottom interface of the FASnI$_3$ absorber and accelerate hole extraction in the inverted tin PSCs, resulting in a large V_{OC} enhancement [32]. Moreover, recently, a wide-bandgap two-dimensional anilinium-based tin perovskite capping layer was constructed atop the FASnI$_3$ absorber via sequential solution deposition method, yielding an increase of the carrier lifetime by about 20 times and a high V_{OC} approaching 0.7 V [15]. In addition to occurring at the surface, charge recombination occurring

inside the tin perovskite crystal seems to be a more critical limitation for V_{OC} improvement because the bulk defects of tin perovskite are two orders of magnitude (10^{15}–10^{16} cm^{-3}) larger than those of lead perovskite (10^{13}–10^{14} cm^{-3}) [27]. However, a strategy to suppress charge recombination in the bulk of the tin perovskite is still lacking. Therefore, advanced bulk passivation technology for tin PSCs should be employed to further improve its efficiency.

Enhancing the built-in electric field in the light-absorbing layer is regarded as an efficient way to reduce charge recombination in the bulk for many thin-film photovoltaic technologies such as organic solar cells, quantum dot solar cells, and Cu(In,Ga)Se$_2$ (CIGS) solar cells [33–37]. For tin halide perovskite absorbers, a Sn^{2+}-poor condition causes a downshift of the Fermi level (E_F) and enables a unipolar p-type characteristic with a very high hole concentration, while a Sn^{2+}-rich condition effectively increases the electron density and tunes the characteristics of tin perovskite from p-type to an intrinsic or relatively n-type semiconductor with a higher E_F position [38–43]. This unique self-doping property allows the production of a localized E_F difference inside the tin perovskite absorber by realizing a heterogeneous distribution of Sn^{2+} to enhance the electric field and further reduce the bulk recombination loss in tin PSCs.

To date, creating a vertical halide gradient (I and Br) or organic cation gradient (phenethylammonium and guanidinium) has been reported for tuning the vertical band structure and E_F alignment in nanoscale-thickness perovskite absorbers, leading to improved efficiency of PSCs [44–46]. Herein, we describe a FASnI$_3$ absorber fabricated with a Sn^{2+} gradient in the vertical direction to minimize carrier recombination loss in the bulk and further improve the device efficiency by enhancing the built-in electric field. This vertical Sn^{2+} gradient was realized by recrystallization of the as-prepared FASnI$_3$ perovskite assisted by a polymethyl methacrylate (PMMA) layer inserted on the upper surface. During the recrystallization process, the carboxylate groups on PMMA could form strong coordination bonds with the Sn^{2+} cations and enrich the Sn^{2+} on the FASnI$_3$ surface. Time-of-flight secondary ion mass spectrometry (Tof–SIMS) and depth-dependent X-ray photoelectron spectroscopy (XPS) revealed that E_F increases with increasing Sn^{2+} content from the bottom to the top in the heterogeneous FASnI$_3$ film, leading to an additional electric field to

assist charge detrapping from bulk defects and accelerate the oriented separation of photo-induced electrons and holes. Consequently, this Sn^{2+}-gradient $FASnI_3$ absorber boosts the PCE of inverted tin PSCs from 10.89 to 13.82% with a V_{OC} increase of 130 mV, and the optimized device still shows a PCE of over 13% after operation under 1-sun illumination for 1,000 h. This study provides a promising route to further improve the PCE of tin PSCs by carefully controlling the built-in electric field in the tin perovskite absorbers.

2 Experimental Section

2.1 Tin PSC Fabrication

The indium tin oxide (ITO) glass substrates were first patterned and cleaned by sequential ultrasonic cleaning with acetone and isopropanol for 10 min and then treated with a UV-ozone cleaner for 30 min before the deposition of polyethylene glycol-poly(3,4-ethylenedioxythiophene):polystyrene sulfonate (PEG-PEDOT:PSS) as the hole transport layer (HTL), as demonstrated in our previous report [47]. To prepare the perovskite precursor solution, formamidinium iodide (FAI), ethylenediammonium diiodide (EDAI$_2$), SnI$_2$, and SnF$_2$ were added to the dimethyl sulfoxide (DMSO) solvent at a molar ratio of 0.99: 0.005: 1: 0.06, with a total concentration of 0.9 M. Then, the perovskite precursor solution was spin-coated onto the ITO glass at 1,000 rpm for 10 s and then 5,000 rpm for 50 s, after which chlorobenzene anti-solvent was dripped onto the tin perovskite film for 30 s. The resulting films were then annealed at 100 °C for 12 min. Subsequently, 0.005 mg mL^{-1} PMMA in chlorobenzene was spin-coated onto the $FASnI_3$ layer at 3,000 rpm. For the recrystallization process, the as-prepared $FASnI_3$ film was placed on a hotplate (60 °C) covered with a petri dish, and 50 μL DMSO was dropped near the film at a distance of 1 cm. Finally, C$_{60}$ (45 nm), bathocuproine (BCP, 5 nm), and an Ag electrode (80 nm) were sequentially evaporated onto the tin perovskite layer under a high vacuum of 2×10^{-5} Pa.

2.2 Film Characterization

Scanning electron microscopy (SEM) images and energy-dispersive X-ray spectroscopy (EDS) were obtained using a Hitachi SU8000 field-emission scanning electron microscope (Japan). To prevent interference from extra elemental Sn signals from the ITO substrate, the $FASnI_3$ films were fabricated on a silicon substrate for Tof–SIMS and EDS measurements. Tof–SIMS measurements were performed using a focused ion-beam Tof–SIMS spectrometer (GAIA3 GMU Model, Czech Republic). A 30 keV Bi$^+$ ion beam was used as the primary ion beam to peel the samples with an analysis area of 5×5 μm^2. X-ray diffraction (XRD) patterns were measured on a Rigaku powder X-ray diffractometer (Japan) using a Cu Kα radiation source at a scan rate of 5° min^{-1}. UV–Vis absorption spectra of the tin perovskite films were recorded using a Shimadzu spectrometer (Japan). Time-resolved photoluminescence (TRPL) analysis was performed using a Hamamatsu C12132 fluorescence lifetime spectrometer (Japan) at an excitation wavelength of 450 nm. Photoelectron spectroscopy in air (PESA) was performed using a Riken Keiki AC-3 instrument (Japan). XPS analysis was performed on a Kratos AXIS Ultra DLD spectrometer (UK) with an Al Kα X-ray source, and an Ar$^+$ source was used to etch the tin perovskite film for detecting the depth profiles of E_F. Grazing incident X-ray diffraction (GIXRD) patterns were measured with a Bruker powder X-ray diffractometer (Germany) using Cu Kα radiation. Scanning Kelvin probe microscopy (SKPM) measurements were performed by an atomic force microscope (AFM, Asylum Research MFP-3D, Oxford Instruments) using Ti/Ir coated Si cantilevers with a nominal spring constant of 2 N m^{-1} (Model: ASYELEC-01). For the SKPM measurements, a Nap mode was used with a DC bias voltage applied to the AFM tip to determine the contact potential difference between the AFM tip and the sample surface.

2.3 Device Characterization

Dark current curves were measured using a DC source monitor (ADC Corporation, 6244, Japan). The J–V curves of the tin PSCs were measured using a solar simulator with a standard air mass of 1.5 sunlight (100 mW cm^{-2}, WXS-155S-10, Wacom Denso, Japan). The active area was defined with a 0.09 cm^2 mask. Monochromatic incident photon-to-current efficiency (IPCE) spectra were measured with monochromatic incident light (1×10^{16} photons cm^{-2}) in the director current mode (CEP-2000BX, Bunko-Keiki). The light intensity of the solar simulator was calibrated using a standard

silicon solar cell. The Mott–Schottky curves of the tin PSCs were measured on a multifunctional electrochemical workstation (Zahner, Germany), with a constant scanning voltage step of 20 mV. All tin PSCs that underwent the stability test were encapsulated according to the process described in our previous study [48]. First, the perovskite from the working area was wiped out using a mixed solvent of dimethylformamide and methanol; then, the cells in N_2 were encapsulated by cavity glass with UV glue on the edges of the working area. Finally, the UV glue was fixed under UV light for 20 s.

3 Results and Discussion

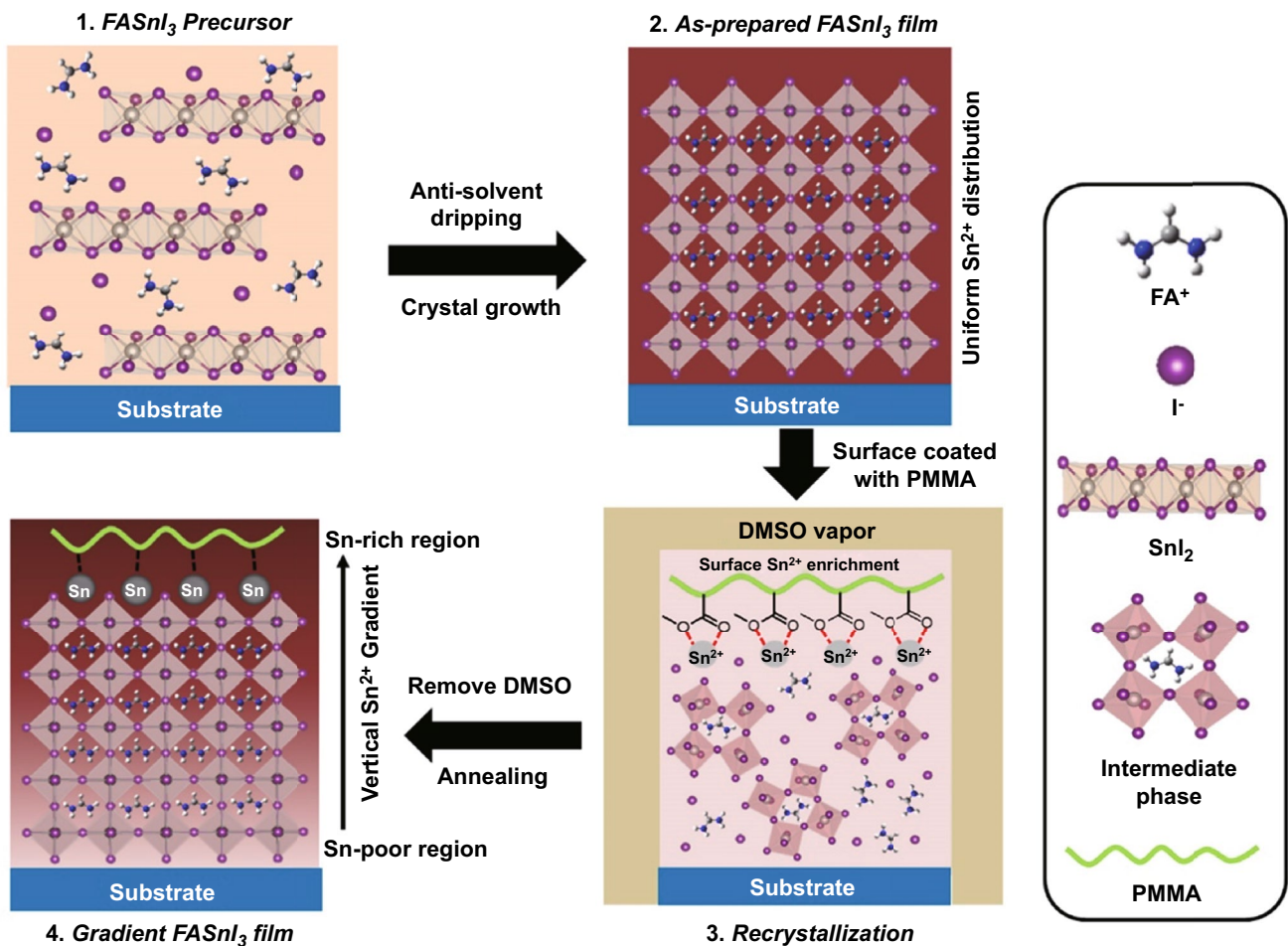### 3.1 Construction of the $FASnI_3$ Absorber with Vertical Sn^{2+} Gradient

The fabrication process of the $FASnI_3$ absorber with a vertical Sn^{2+} gradient is illustrated in Fig. 1. In the first step, the $FASnI_3$ precursor solution was dropped onto the substrate, and a certain amount of $EDAI_2$ was employed as an additive to improve the crystallinity and reduce the pinholes of the $FASnI_3$ perovskite [49]. After the induction of crystal growth thermal annealing, a $FASnI_3$ film with a uniform Sn^{2+} distribution is supposed to be formed. Subsequently, we spin-coated a Lewis base-rich polymer, PMMA, on the surface and then treated the as-prepared PMMA-coated $FASnI_3$ film with DMSO vapor to form an intermediate wet film, leading to recrystallization of the $FASnI_3$ perovskite. In the $FASnI_3$-DMSO intermediate film, Sn^{2+} tends to be enriched on the top surface because of the strong coordination interactions formed between the carboxylate groups (O=C–O) and Sn^{2+} cations [50], resulting in a gradient Sn^{2+} distribution in the vertical direction after the second annealing process. In the following discussion, we denote the $FASnI_3$ film without any modification as "$FASnI_3$" control and the $FASnI_3$ film with both PMMA coating and DMSO-vapor treatment as "$FASnI_3$ gradient." For comparison, we also prepared an $FASnI_3$ film with PMMA coating but without DMSO-vapor treatment (denoted as PMMA coating) and a film with DMSO-vapor treatment but without PMMA coating (denoted as DMSO-vapor treatment).

The coordination interaction between Sn^{2+} and the carboxylate group was confirmed using Fourier transform infrared (FTIR) spectroscopy. As shown in Fig. 2a,

both the vibration signals of the C=O and C–O–C groups shifted to a smaller wavenumber after being mixed with the SnI_2 precursor, attributed to the deformation of the electron cloud and reduced bond stiffness induced by the formation of bidentate coordination. After thermal annealing, the intermediate phase with PMMA is expected to form a solid-state $FASnI_3$ film with a gradient increase in elemental Sn from the bottom to the surface.

The reason for choosing PMMA as the Sn^{2+}-enrichment additive is that each PMMA monomer contains a carboxylate group that could form bidentate coordination with Sn^{2+}, and such high-concentration Lewis base groups could extract a certain amount of Sn^{2+} to the surface in the $FASnI_3$ wet film during recrystallization. Furthermore, unlike other small-molecule additives, the large-size PMMA cannot permeate into the bottom of the $FASnI_3$ film, which ensures that the Sn-enrichment process only occurs at the top surface of the film.

First, we investigated the effect of the DMSO-induced recrystallization process on the surface morphology of the $FASnI_3$ perovskite films. Figure S1 shows top-view SEM images of the $FASnI_3$ films after exposure to DMSO vapor for different times. It can be observed that the $FASnI_3$ film maintained a compact polycrystalline morphology when the exposure time was less than 5 s. In contrast, a longer exposure time led to many pinholes being formed at the grain boundary, and an island-like structure was formed after 15 s exposure to DMSO vapor, indicating serious corrosion of the $FASnI_3$ crystal by DMSO vapor. In addition, the XRD patterns of the intermediate film (gray color) after 5 s DMSO exposure and the film after the second annealing (black color) are depicted in Fig. S2a; the intermediate film exhibited an unordered amorphous structure without obvious diffraction peaks, and the peak at 14.0° (perovskite phase) appeared after the re-annealing process, which confirmed that the recrystallization process had occurred. Then, we measured the XRD patterns of the $FASnI_3$ films undergoing recrystallization with different DMSO exposure times to understand the effect of DMSO vapor on crystallinity, as shown in Fig. S2b. It was found that the $FASnI_3$ film treated with DMSO vapor for up to 5 s maintained the same intensity of the (100) and (200) diffraction peaks at 14.0° and 28.2° compared to the fresh sample, but a longer DMSO treatment time significantly reduced the film crystallinity. Consequently, we chose an exposure time of 5 s for

1. *FASnI_3 Precursor*

2. *As-prepared FASnI_3 film*

Anti-solvent dripping

Crystal growth

Uniform Sn^{2+} distribution

Substrate

Substrate

FA$^+$

I$^-$

SnI$_2$

Surface coated with PMMA

Sn-rich region

Sn Sn Sn Sn

Vertical Sn^{2+} Gradient

Remove DMSO

Annealing

Sn-poor region

Substrate

4. *Gradient FASnI_3 film*

DMSO vapor

Surface Sn^{2+} enrichment

Sn^{2+} Sn^{2+} Sn^{2+} Sn^{2+}

Substrate

3. *Recrystallization*

Intermediate phase

PMMA

Fig. 1 Schematic of the fabrication of gradient FASnI$_3$ film with an increased Sn^{2+} content from bottom to top by recrystallization of the as-prepared FASnI$_3$ perovskite film assisted with surface-coated PMMA with a high concentration of carboxylate groups

the recrystallization process to fabricate the gradient FASnI$_3$ perovskite film in subsequent studies.

3.2 Vertical Composition Analysis of the FASnI$_3$ Gradient Film

To investigate the vertical elemental distribution, we measured the Tof–SIMS depth profiles of the control and gradient films deposited on a Si substrate to avoid the effect of the outside Sn signal from the ITO glass. As shown in Fig. 2b, the intensities of the Sn and I signals remained almost the same in the vertical direction in the control sample, indicating that the Sn^{2+} distribution was homogeneous. In contrast, the intensity of the Sn signal in the gradient film increased gradually during the first 50 s of sputtering time, whereas

the I signal did not show any obvious change (Fig. 2c), indicating that a Sn-rich region formed at the upper part and a Sn-poor region at the bottom (from 250 to 330 s). Moreover, Tof–SIMS two-dimensional mapping profiles of elemental Sn along the *x–z* plane were applied to visualize the top Sn-rich region (indicated by dark red) and the bottom Sn-poor region (indicated by light blue) in the FASnI$_3$ gradient film (Fig. 2d). In contrast, the control FASnI$_3$ film exhibited a uniform color-mapping profile. We then calculated the top and bottom Sn/I ratios in the FASnI$_3$ gradient film using energy-dispersive spectrometry (EDS). As shown in Fig. 2e, the top Sn/I ratio was calculated to be 1.08:3 according to the EDS point profile, which is larger than 1:3 in the ideal FASnI$_3$ perovskite crystal. In contrast, the bottom Sn/I ratio was calculated to be 0.94:3 (Fig. 2f), indicating that a Sn-poor condition was formed in the bottom region. For
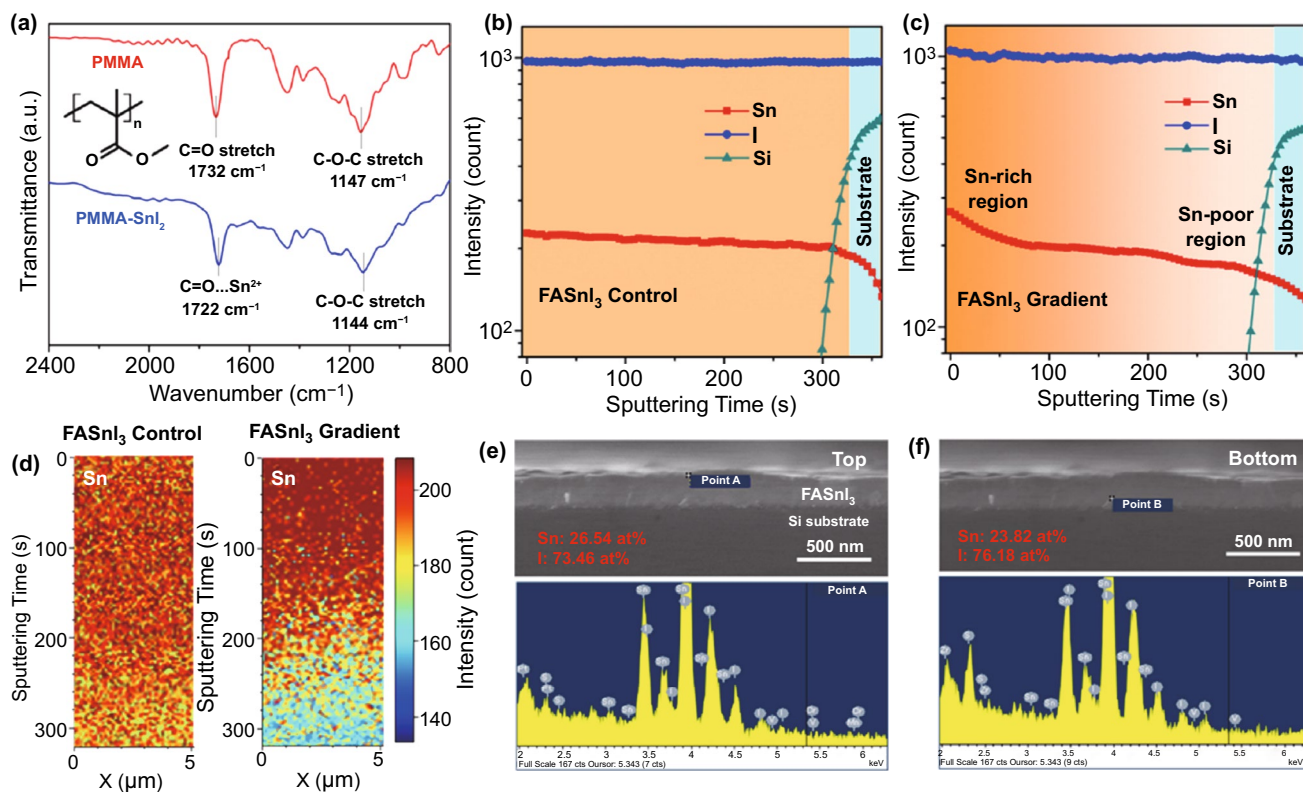
Fig. 2 **a** FTIR spectroscopy of the pure PMMA and PMMA-SnI$_2$ mixture. Tof–SIMS depth profiles of the Sn, I, and Si elements in **b** FASnI$_3$ control and **c** FASnI$_3$ gradient films coated on the silicon substrate. **d** Tof–SIMS two-dimensional mapping profiles of Sn along the x–z plane for the FASnI$_3$ control and FASnI$_3$ gradient films. Cross-sectional SEM images and EDS point profiles derived from the **e** top and **f** bottom of gradient film

comparison, we also estimated the Sn/I ratio of the control film using EDS analysis (Fig. S3a-b). The top and bottom Sn/I ratios were calculated to be 1.04:3 and 1.03:3, respectively, indicating homogeneous elemental distribution in the pristine FASnI$_3$ film. We consider that the deviation of the Sn/I ratio from the ideal value (1:3) in the FASnI$_3$ control film is ascribed to the presence of extra SnF$_2$, which is a commonly used antioxidant additive in high-performance tin PSCs [51].

Subsequently, GIXRD analysis was conducted to study the effect of the vertical compositional gradient on the lattice parameters of the FASnI$_3$ films. As shown in Fig. S4, no obvious change in the position of the (100) diffraction peak was found in the FASnI$_3$ gradient film when the X-ray incident angle increased from 0.2° to 1.0°, which means that the self-doping effect of excess Sn^{2+} or Sn vacancies did not cause a significant lattice distortion of the corner-sharing FASnI$_3$ perovskite crystal, reducing the phase stability.

3.3 Optical and Electronic Property of the FASnI$_3$ Gradient Film

We then studied the effect of this vertical Sn^{2+} gradient on the optical and electronic properties of the FASnI$_3$ perovskite films. As can be seen in Fig. S5a, the FASnI$_3$ gradient sample exhibited a similar absorption in the visible light region to the control sample, indicating that the self-doping effect had a negligible influence on the light-harvesting ability of FASnI$_3$ absorbers. Based on the Tauc plots in Fig. S5b, the bandgaps of the FASnI$_3$ control and gradient films were calculated to be 1.42 and 1.41 eV, respectively, which were consistent with those reported in a previous study [50]. We also investigated the effect of Sn-rich and Sn-poor conditions on the bandgap of FASnI$_3$ films by fabricating a FASnI$_3$ film with excess SnI$_2$ (7.7 mol%) and FAI (6.3 mol%) to reach the same Sn/I stoichiometric ratio of the top and bottom regions of FASnI$_3$ gradient film.

Both the Sn-rich and Sn-poor FASnI$_3$ films showed a bandgap at approximately ~ 1.41 to 1.42 eV, indicating negligible bandgap fluctuation (less than 0.01 eV) in the vertical direction of the FASnI$_3$ gradient film. Subsequently, we measured the valence band maximum (VBM) using PESA to understand the band structure of the FASnI$_3$ control and gradient films. As shown in Fig. S5c, the VBM of control and gradient samples were calculated to be − 4.91 and − 4.93 eV, respectively. In addition, the PESA plots in Fig. S5d confirmed that the Sn-rich and Sn-poor conditions did not influence the VBM position of the FASnI$_3$ gradient perovskite. After deducing the bandgap value, we calculated the conduction band minimum (CBM) of the control and gradient films to be − 3.49 and − 3.51 eV, respectively.

Furthermore, we used an Ar$^+$ source to etch the FASnI$_3$ films and measured the E_F at different etching times via valence-band XPS analysis to study the depth profile of the Fermi level. As shown in Fig. 3a, the distance between VBM and E_F was calculated to be approximately ~ 0.67 to 0.69 eV for the entire FASnI$_3$ control film. By contrast, this value decreased from 0.85 (top) to 0.54 eV (bottom) in FASnI$_3$ gradient film, indicating an E_F difference of about 0.3 eV in the monolithic perovskite film (Fig. 3b). To illustrate this vertical E_F gradient, we derived the depth profiles of the E_F shown in Fig. 3c using valence-band XPS analysis. It can be seen that the E_F with respect to the vacuum level of control film locate at approximately − 4.20 to − 4.22 eV, associated with an intrinsic-semiconductor characteristic without extra doping. In the case of FASnI$_3$ gradient film, a gradual decrease of E_F from − 4.11 to − 4.42 eV was found, indicating n-type doping at the top region and p-type doping at the bottom region regarding the constant VBM and CBM values in the vertical direction of the gradient film. In addition, it is worth noting that the E_F change at the top was larger than that at the bottom in the FASnI$_3$ gradient film, which was consistent with the trend of the vertical Sn^{2+} distribution derived from the Tof–SIMS measurement.

Based on this E_F depth profile, we drew a possible band structure and charge trapping model for the FASnI$_3$ control (Fig. 3d) and gradient (Fig. 3e) absorbers. For the control film, no obvious band bending was formed owing to the homogeneous E_F distribution, and the charge extraction force mainly came from the energy offset at the electron-selective or hole-selective interfaces. In this regard, carriers inside the perovskite crystal can be easily trapped by

the bulk defects. In contrast, the E_F difference ($\triangle E_F$) in the FASnI$_3$ gradient film caused downward band bending at the top electron-selective interface and upward band bending at the bottom hole-selective interface, generating an extra built-in electric field in the FASnI$_3$ absorber to retard charge trapping by the bulk defects and promote oriented charge transport and extraction, resulting in a lower recombination loss inside the FASnI$_3$ absorber [52]. However, the surface high-resolution C 1 s XPS spectra (Fig. S6) showed additional peaks at 287.1 eV (C–O–C group) and 288.0 eV (O=C–O group) in the FASnI$_3$ gradient sample [53], indicating the presence of PMMA on the surface after recrystallization, which could further induce surface passivation to reduce non-radiative recombination loss [54, 55].

3.4 Carrier Separation Dynamics in the FASnI$_3$ Gradient Film

SKPM was used to characterize the surface potential difference of the FASnI$_3$ perovskite under Sn-rich and Sn-poor conditions to further illustrate the Fermi level difference induced by the tin source gradient. As shown in Figs. 4a−c and S7, the control film exhibited an almost uniform surface potential distribution with an AFM tip DC voltage of approximately 100 mV, while a lower AFM tip DC voltage of approximately 50 mV was found for the Sn-poor FASnI$_3$ perovskite (6.3 mol% FAI excess), which can be attributed to hole accumulation that causes a downward shift of the Fermi level towards the valence band. In contrast, for the Sn-rich film (7.7 mol% SnI$_2$ excess) a higher AFM tip DC voltage of approximately 125 mV was observed because of the n-type doping effect, which was consistent with the trend found in the XPS results. Subsequently, we compared the charge extraction capability of the FASnI$_3$ control and FASnI$_3$ gradient films by calculating the decay lifetime of the TRPL spectra (Fig. 4d–e). The average decay lifetime (τ_{ave}) was calculated using the double-exponential decay equation, and the fitting parameters are summarized in Table S1. We found that the τ_{ave} of the control film decreased from 4.82 to 1.85 ns and 2.46 ns after the incorporation of HTL PEDOT:PSS and electron transport layer (ETL) fullerene C$_{60}$, respectively. By contrast, the τ_{ave} values of FASnI$_3$ gradient, PEDOT/FASnI$_3$ gradient, and FASnI$_3$ gradient/C$_{60}$ films were calculated to be 6.98, 1.05, and 1.23 ns, respectively. To understand the increased τ_{ave} in the gradient film, we measured the TRPL
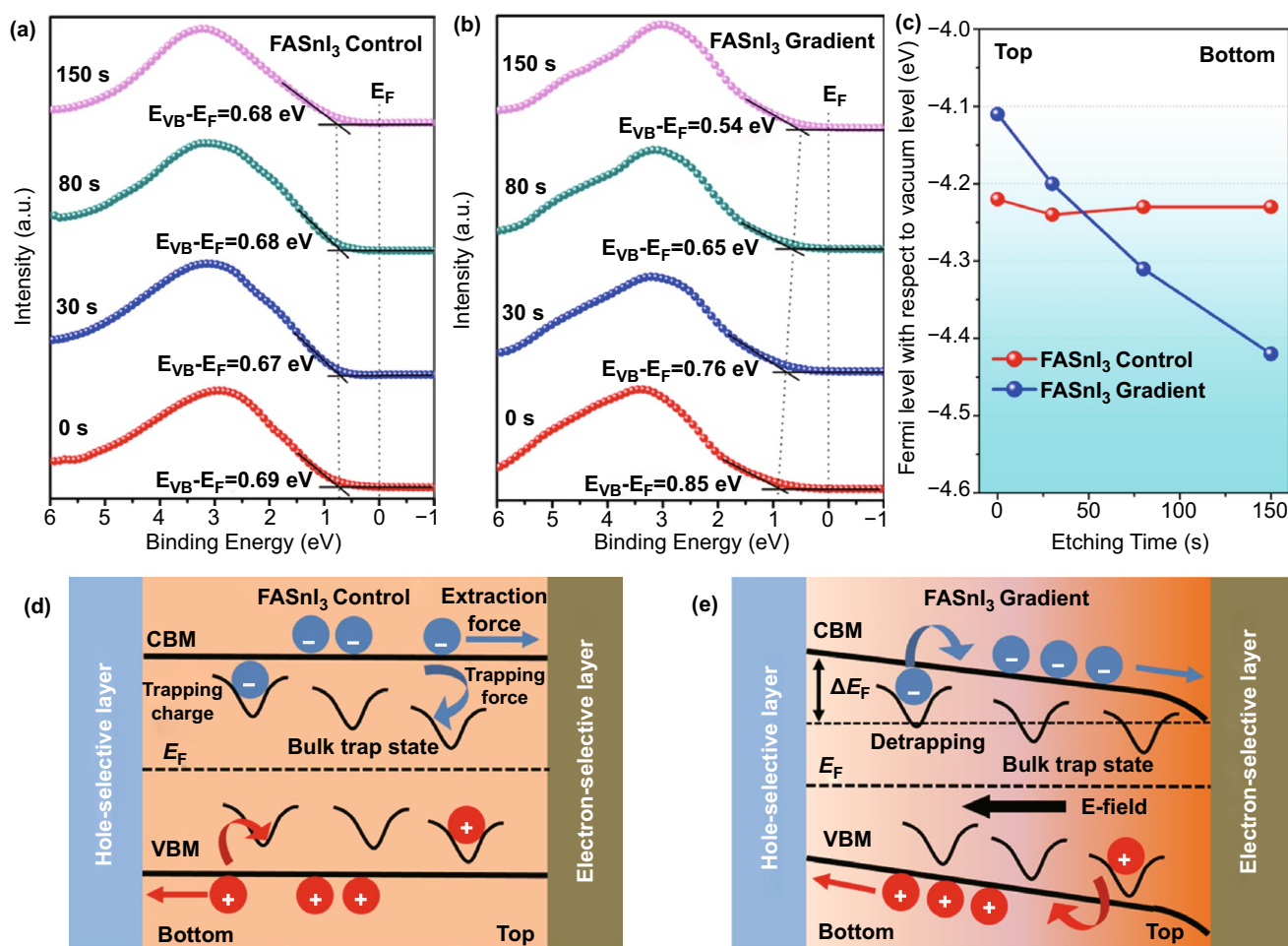
Fig. 3 The valence-band XPS spectra of the **a** FASnI$_3$ control and **b** FASnI$_3$ gradient films with different Ar$^+$ etching time. **c** Depth profiles of the E_F in FASnI$_3$ control and FASnI$_3$ gradient films derived from the valence-band XPS analysis. Predicted energy-level diagram and charge trapping model in the **d** FASnI$_3$ control and **e** FASnI$_3$ gradient films in contact with the electron-selective and hole-selective layers

plots of the FASnI$_3$ film with a coating of only PMMA. As seen in Fig. S8, the PMMA coating film exhibited a similar τ_{ave} of 6.75 ns but a lower carrier extraction efficiency at the charge-selective interfaces compared to those of the gradient film. These results indicate that the improvement in τ_{ave} was mainly caused by the surface passivation effect of PMMA [56], and the improvement in the charge extraction efficiency can be attributed to the formation of a vertical Sn^{2+}-gradient architecture. Additionally, we measured the dark current of the FASnI$_3$ perovskite layer sandwiched between the two electrodes to characterize the difference in the electronic properties induced by the self-doping effect (Fig. 4f). The control sample showed a symmetric current plot at the positive and negative biases, whereas the gradient sample exhibited an asymmetric current plot with a much larger current output at the positive bias, indicating the formation of a depletion layer inside the gradient FASnI$_3$ absorber, further confirming the formation of a built-in electric field induced by the vertical Sn^{2+} gradient.

3.5 Oxidation Property of the FASnI$_3$ Gradient Film

We investigated the effect of the vertical Sn^{2+} gradient on the oxidation properties of the FASnI$_3$ absorber by tracking the changes in the Sn $3d$ XPS spectra before and after 3 h aging in air. As seen in Fig. S9a-b, approximately 76% of the Sn^{2+} cations were oxidized to Sn^{4+} in the FASnI$_3$ control film, whereas 53% of the Sn^{2+} cations were oxidized to Sn^{4+} (Fig. S9c-d) in the gradient films.
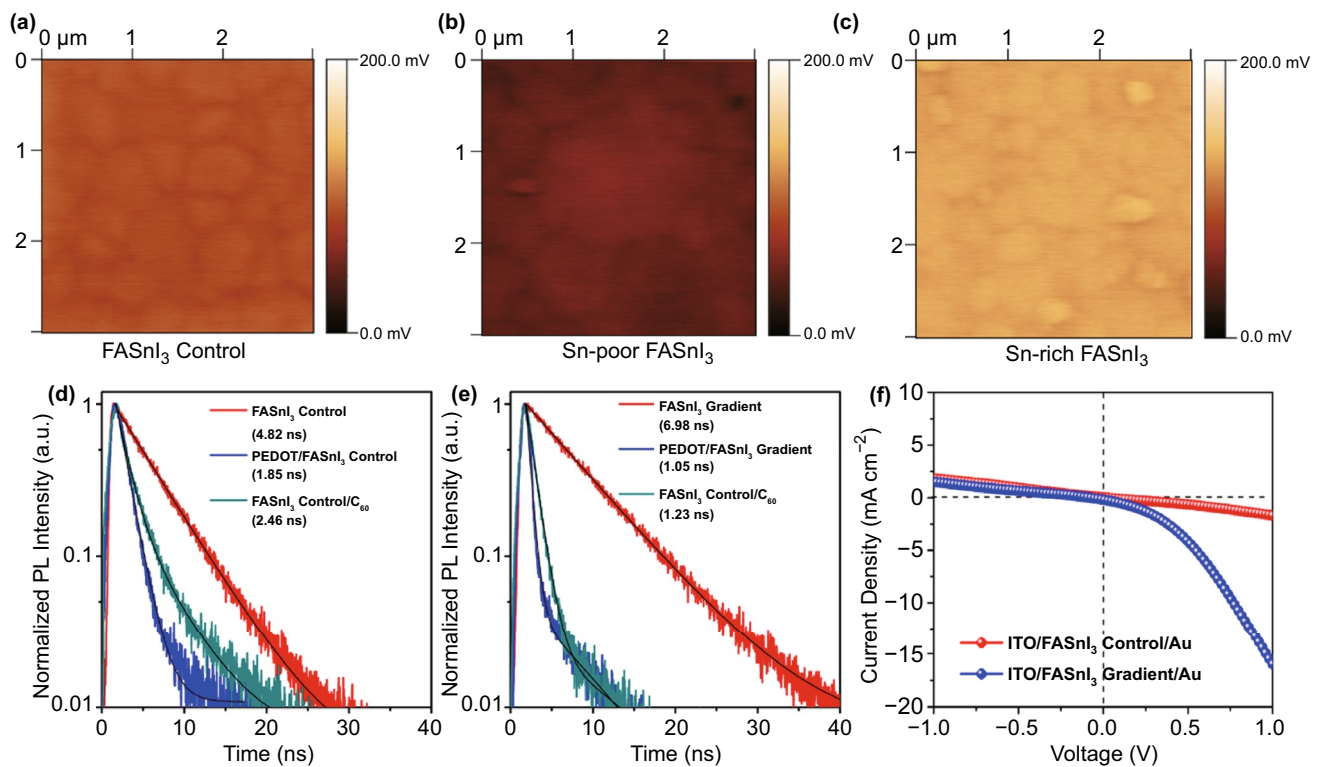
Fig. 4 Surface potential mapping images of the **a** control, **b** Sn-poor, and **c** Sn-rich FASnI$_3$ perovskite films deposited on the PEDOT:PSS/ITO substrate. TRPL spectra of the **d** control and **e** gradient FASnI$_3$ films coated on the quartz substrate before and after contact with C$_{60}$ or PEDOT:PSS layers. **f** Output dark current plots as a function of the applied voltage for the ITO/FASnI$_3$ control/Au and the ITO/FASnI$_3$ gradient/Au devices

We deduced that this slower oxidation process could be due to the Sn-rich environment of the tin perovskite crystal significantly increasing the chemical potential of elemental Sn (μ_{Sn}), which in turn increases the formation energy of Sn vacancies and therefore retards the oxidation reaction from Sn^{2+} to Sn^{4+} and Sn vacancies [39, 57].

3.6 Performance of the Tin Perovskite Solar Cells

To study the effect of the gradient FASnI$_3$ absorber on the PV performance of tin PSCs, we fabricated inverted planar solar cells with an ITO/ PEDOT:PSS/FASnI$_3$ gradient absorber/C$_{60}$/BCP/Ag electrode structure (Fig. 5a). The cross-sectional SEM image of the FASnI$_3$ gradient inverted PSCs (Fig. 5b) shows that a compact FASnI$_3$ film with an average thickness of 230 nm was formed on the ITO/PEDOT:PSS substrate, while a 50-nm-thick electron-selective C$_{60}$/BCP bilayer was deposited atop the FASnI$_3$ perovskite. For comparison, the same structure was applied

to the FASnI$_3$ control cell with a 226-nm-thick perovskite absorber (the cross-sectional SEM image is shown in Fig. S10). We first compared the current density–voltage (J–V) curves of the FASnI$_3$ control device, FASnI$_3$ gradient device, device with only DMSO-vapor treatment, and device with only PMMA coating, as shown in Figs. 5c and S11a (the corresponding PV parameters are summarized in Tables 1 and S2). The PCEs of the control device were calculated as 10.52% and 10.89%, with short-circuit current density (J_{SC}) of 21.88 and 21.81 mA cm^{-2}, V_{OC} of 0.71 and 0.73 V, and fill factor (FF) of 67.7% and 68.4% under the forward and reverse scans, respectively. In contrast, the FASnI$_3$ gradient devices showed much higher PCEs of 13.61% and 13.82%, with J_{SC} of 22.87 and 22.74 mA cm^{-2}, V_{OC} of 0.84 and 0.85 V, and FF of 70.9% and 71.5% under the forward and reverse scans, respectively. These PCE values of the gradient FASnI$_3$ PSCs were comparable with those of the state-of-the-art tin PSCs in previous studies (the PV parameters are summarized in Table S3). In contrast, the FASnI$_3$ PSCs with

only DMSO-vapor treatment showed a negligible efficiency improvement (10.87% under forward scan and 11.07% under reverse scan), and the Tof–SIMS two-dimensional mapping profile indicated a uniform vertical Sn^{2+} distribution in the perovskite absorber (Fig. S11b). These results revealed that DMSO-induced recrystallization without PMMA assistance

could not create a Sn^{2+} gradient to enhance the electric field and boost the tin PSC performance. In addition, the PSCs with only PMMA coating showed PCEs of 11.36% (forward scan) and 11.65% (reverse scan) with a slight increase in V_{OC} (approximately 40 mV). The above analysis indicates that the J_{SC} improvement in the $FASnI_3$ gradient
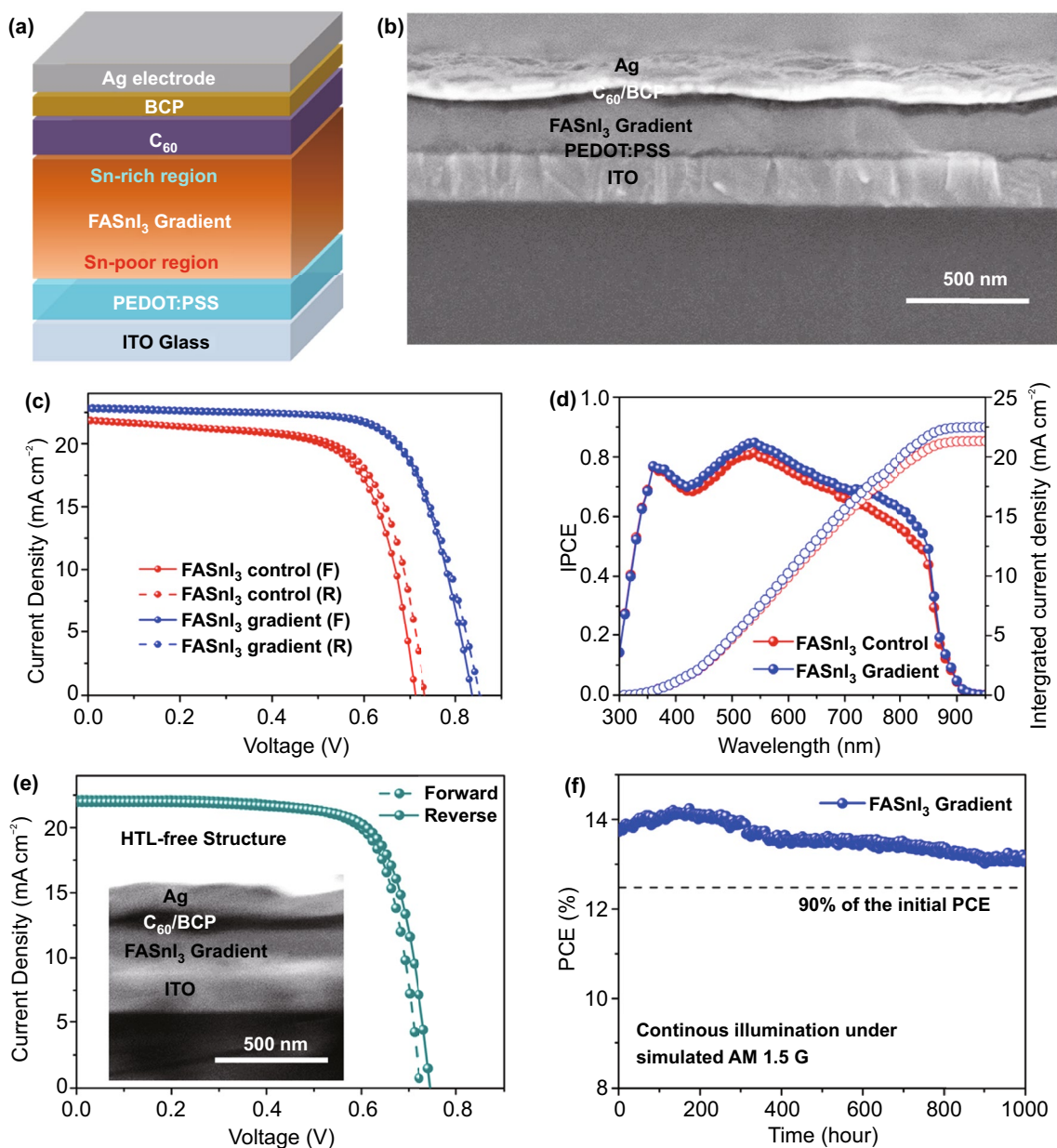
Fig. 5 **a** Schematic illustration of the gradient $FASnI_3$-based inverted PSCs and **b** the corresponding device cross-sectional SEM image. **c** Forward and reverse J–V curves of the best-performing $FASnI_3$ control and gradient PSCs. **d** IPCE spectra and the integrated current density of the $FASnI_3$ control and gradient devices. **e** Forward and reverse J–V curves of the HTL-free $FASnI_3$ gradient device (the inset shows the cross-section of the SEM image). **f** Operational stability test of the encapsulated $FASnI_3$ gradient PSC under simulated AM 1.5G light in air

device was induced by the Sn^{2+}-gradient architecture with an enhanced electric field, and the V_{OC} improvement was caused by the synergistic effect of the PMMA passivation and Sn^{2+}-gradient architecture.

To confirm the reliability of the J–V measurements, the IPCE spectra of the control and gradient FASnI$_3$ PSCs were measured (Fig. 5d). The integrated J_{SC} of the FASnI$_3$ control and gradient cells were calculated to be 21.39 and 22.47 mA cm^{-2}, respectively. These J_{SC} values were close to those of the J–V measurements. In addition, we found that the IPCE increased significantly in the range of 700–850 nm when a gradient FASnI$_3$ absorber was incorporated, this IPCE increase of gradient FASnI$_3$ was associated with improvement in carrier extraction efficiency at the back interface, which is caused by the large downward band bending at the gradient FASnI$_3$/C$_{60}$ interface that promotes the electron extraction process.

To study the reproducibility of the FASnI$_3$ control and gradient PSCs, we fabricated 40 cells for each kind of device. The control devices showed an average PCE of 9.83% with a standard deviation of 0.62% (Fig. S12). In contrast, the average PCE of the FASnI$_3$ gradient device was calculated to be 13.12%, with a smaller standard deviation of 0.49%. These results further confirmed the high reproducibility of the PMMA-assisted recrystallization method for fabricating high-performance tin PSCs.

In addition, Mott–Schottky analysis was applied to investigate the built-in potential in the FASnI$_3$ control and gradient PSCs. As shown in Fig. S13, we derived the built-in potential results from the Mott–Schottky plots by calculating their intercepts at the x-axis and found that the built-in potential of the gradient tin PSCs was approximately

0.14 V higher than that of the control PSCs, which was consistent with the V_{OC} improvement demonstrated by the J–V tests (Fig. 5c).

We further fabricated an HTL-free FASnI$_3$ gradient PSC to emphasize its unique charge separation capability by directly removing the PEDOT:PSS layer. As seen in Fig. 5e, the HTL-free gradient device could still maintain a similar photocurrent to the completed cell (the integrated J_{SC} was calculated as 22.13 mA cm^{-2} in the IPCE spectrum shown in Fig. S14) and exhibited efficiencies of 11.61% and 11.91% with FF values of 71.9% and 72.3% under the forward and reverse scans, respectively. The higher FF was attributed to the reduced series resistance for hole transport in the HTL-free PSCs. It is worth noting that this is the highest PCE value reported for HTL-free tin PSCs to date. (A comparison of the HTL-free device performance between this and previous studies is presented in Table S4.)

Stability is another important criterion for the commercialization of tin PSCs. In the present study, we tracked the operational stability of the best-performing FASnI$_3$ gradient cell under simulated AM 1.5G light (100 mW cm^{-2}) at the maximum power point in air. As shown in Fig. 5f, the FASnI$_3$ gradient cell exhibited an initial power output of 13.80%. Interestingly, the power output gradually increased to over 14% at an operational time of 100 h and this high power output was maintained for approximately 200 h before an obvious PCE drop. This PCE improvement induced by the light-soaking effect will be further investigated in the future. After 1,000 h of operation, we found that the PCE of the FASnI$_3$ gradient cell was maintained at over 13%, indicating that the surface Sn-rich region could serve as a protective layer to suppress oxygen-induced degradation of tin perovskite crystals. For comparison, we also measured the operational stability of the FASnI$_3$ control PSCs and observed a large PCE loss of more than 20% after 500 h operation at the maximum power point (Fig. S15), which was associated with the relatively poor long-term stability of the control device. In addition, we measured the thermal stabilities of the control and gradient cells. As shown in Fig. S16, both devices showed an efficiency loss of approximately 5% after heating at 60 °C in a N$_2$ atmosphere for 100 h, indicating that such an inverted device structure is stable under thermal aging.

Table 1 The PV parameters of the FASnI$_3$ control, FASnI$_3$ gradient, FASnI$_3$ with the surface passivation of PMMA, as well as the HTL-free FASnI$_3$ gradient PSCs

Samples	Scan Direction	J_{SC} (mA cm^{-2})	V_{OC} (V)	FF (%)	PCE (%)
FASnI$_3$ control	Forward	21.88	0.71	67.7	10.52
	Reverse	21.81	0.73	68.4	10.89
FASnI$_3$ gradient	Forward	22.87	0.84	70.9	13.61
	Reverse	22.74	0.85	71.5	13.82
FASnI$_3$ gradient (HTL-free structure)	Forward	21.21	0.73	71.9	11.61
	Reverse	21.39	0.75	72.3	11.91

4 Conclusion

In summary, we propose a novel recrystallization strategy to fabricate a gradient $FASnI_3$ perovskite absorber with an enhanced built-in electric field to minimize both bulk and surface charge recombination losses in tin PSCs. The top Sn-rich and bottom Sn-poor regions caused a large E_F difference, which generated an additional electric field inside the tin perovskite layer to separate the photo-induced electrons and holes. As a result, the $FASnI_3$ absorber with a vertical Sn^{2+} gradient exhibited a promising efficiency of 13.82% for inverted $FASnI_3$-based PSCs, which is one of the highest PCEs reported for lead-free perovskite solar cells to date. Gradient tin PSCs are ultrastable, maintaining over 13% efficiency after operation at 1-sun illumination for 1,000 h. More importantly, the present study provides a universal way to further improve the performance of tin PSCs in the future because it is suitable for all kinds of Sn or mixed Sn–Pb perovskite compositions.

Supplementary Information The online version contains supplementary material available at https://doi.org/10.1007/s40820-022-00842-4.

References

1. X. Jiang, Z. Zang, Y. Zhou, H. Li, Q. Wei et al., Tin halide perovskite solar cells: an emerging thin-film photovoltaic technology. Acc. Mater. Res. **2**(4), 210–219 (2021). https://doi.org/10.1021/accountsmr.0c00111

2. J. Cao, F. Yan, Recent progress in tin-based perovskite solar cells. Energy Environ. Sci. **14**(3), 1286–1325 (2021). https://doi.org/10.1039/D0EE04007J

3. F. Gu, Z. Zhao, C. Wang, H. Rao, B. Zhao et al., Lead-free tin-based perovskite solar cells: strategies toward high performance. Sol. RRL **3**(9), 1900213 (2019). https://doi.org/10.1002/solr.201900213

4. T. Wu, Z. Qin, Y. Wang, Y. Wu, W. Chen et al., The main progress of perovskite solar cells in 2020–2021. Nano-Micro Lett. **13**(1), 152 (2021). https://doi.org/10.1007/s40820-021-00672-w

5. R. Lin, K. Xiao, Z. Qin, Q. Han, C. Zhang et al., Monolithic all-perovskite tandem solar cells with 24.8% efficiency exploiting comproportionation to suppress sn(ii) oxidation in precursor ink. Nat. Energy **4**(10), 864–873 (2019). https://doi.org/10.1038/s41560-019-0466-3

6. S. Sahare, H.D. Pham, D. Angmo, P. Ghoderao, J. MacLeod et al., Emerging perovskite solar cell technology: Remedial actions for the foremost challenges. Adv. Energy Mater. **11**(42), 2101085 (2021). https://doi.org/10.1002/aenm.202101085

7. X. Jiang, H. Li, Q. Zhou, Q. Wei, M. Wei et al., One-step synthesis of $SnI_2 \cdot (DMSO)_x$ adducts for high-performance tin perovskite solar cells. J. Am. Chem. Soc. **143**(29), 10970–10976 (2021). https://doi.org/10.1021/jacs.1c03032

8. K. Nishimura, M.A. Kamarudin, D. Hirotani, K. Hamada, Q. Shen et al., Lead-free tin-halide perovskite solar cells with 13% efficiency. Nano Energy **74**, 104858 (2020). https://doi.org/10.1016/j.nanoen.2020.104858

9. D. Cui, X. Liu, T. Wu, X. Lin, X. Luo et al., Making room for growing oriented $FASnI_3$ with large grains via cold precursor solution. Adv. Funct. Mater. **31**(25), 2100931 (2021). https://doi.org/10.1002/adfm.202100931

10. B.-B. Yu, Z. Chen, Y. Zhu, Y. Wang, B. Han et al., Heterogeneous 2D/3D tin-halides perovskite solar cells with certified conversion efficiency breaking 14%. Adv. Mater. **33**(36), 2102055 (2021). https://doi.org/10.1002/adma.202102055

11. T. Wu, D. Cui, X. Liu, X. Meng, Y. Wang et al., Efficient and stable tin perovskite solar cells enabled by graded heterostructure of light-absorbing layer. Sol. RRL **4**(9), 2000240 (2020). https://doi.org/10.1002/solr.202000240

12. Y. Liao, H. Liu, W. Zhou, D. Yang, Y. Shang et al., Highly oriented low-dimensional tin halide perovskites with enhanced stability and photovoltaic performance. J. Am. Chem. Soc. **139**(19), 6693–6699 (2017). https://doi.org/10.1021/jacs.7b01815

13. C. Ran, W. Gao, J. Li, J. Xi, L. Li et al., Conjugated organic cations enable efficient self-healing $FASnI_3$ solar cells. Joule **3**(12), 3072–3087 (2019). https://doi.org/10.1016/j.joule.2019.08.023

14. X. Liu, T. Wu, J.-Y. Chen, X. Meng, X. He et al., Templated growth of FASnI$_3$ crystals for efficient tin perovskite solar cells. Energy Environ. Sci. **13**(9), 2896–2902 (2020). https://doi.org/10.1039/d0ee01845g

15. E. Jokar, P.-Y. Cheng, C.-Y. Lin, S. Narra, S. Shahbazi et al., Enhanced performance and stability of 3D/2D tin perovskite solar cells fabricated with a sequential solution deposition. ACS Energy Lett. **6**(2), 485–492 (2021). https://doi.org/10.1021/acsenergylett.0c02305

16. E. Jokar, C.-H. Chien, C.-M. Tsai, A. Fathi, E.W.-G. Diau, Robust tin-based perovskite solar cells with hybrid organic cations to attain efficiency approaching 10%. Adv. Mater. **31**(2), 1804835 (2019). https://doi.org/10.1002/adma.201804835

17. X. Meng, Y. Wang, J. Lin, X. Liu, X. He et al., Surface-controlled oriented growth of FASnI$_3$ crystals for efficient lead-free perovskite solar cells. Joule **4**(4), 902–912 (2020). https://doi.org/10.1016/j.joule.2020.03.007

18. W. Liao, D. Zhao, Y. Yu, C.R. Grice, C. Wang et al., Lead-free inverted planar formamidinium tin triiodide perovskite solar cells achieving power conversion efficiencies up to 6.22%. Adv. Mater. **28**(42), 9333–9340 (2016). https://doi.org/10.1002/adma.201602992

19. X. He, T. Wu, X. Liu, Y. Wang, X. Meng et al., Highly efficient tin perovskite solar cells achieved in a wide oxygen concentration range. J. Mater. Chem. A **8**(5), 2760–2768 (2020). https://doi.org/10.1039/C9TA13159K

20. Q. Tai, X. Guo, G. Tang, P. You, T.-W. Ng et al., Antioxidant grain passivation for air-stable tin-based perovskite solar cells. Angew. Chem. Int. Ed. **58**(3), 806–810 (2019). https://doi.org/10.1002/anie.201811539

21. X. Meng, T. Wu, X. Liu, X. He, T. Noda et al., Highly reproducible and efficient FASnI$_3$ perovskite solar cells fabricated with volatilizable reducing solvent. J. Phys. Chem. Lett. **11**(8), 2965–2971 (2020). https://doi.org/10.1021/acs.jpclett.0c00923

22. E.W.-G. Diau, E. Jokar, M. Rameez, Strategies to improve performance and stability for tin-based perovskite solar cells. ACS Energy Lett. **4**(8), 1930–1937 (2019). https://doi.org/10.1021/acsenergylett.9b01179

23. S. Shao, J. Liu, G. Portale, H.-H. Fang, G.R. Blake et al., Highly reproducible Sn-based hybrid perovskite solar cells with 9% efficiency. Adv. Energy Mater. **8**(4), 1702019 (2018). https://doi.org/10.1002/aenm.201702019

24. K. Chen, P. Wu, W. Yang, R. Su, D. Luo et al., Low-dimensional perovskite interlayer for highly efficient lead-free formamidinium tin iodide perovskite solar cells. Nano Energy **49**, 411–418 (2018). https://doi.org/10.1016/j.nanoen.2018.05.006

25. B. Li, H. Di, B. Chang, R. Yin, L. Fu et al., Efficient passivation strategy on Sn related defects for high performance all-inorganic CsSnI$_3$ perovskite solar cells. Adv. Funct. Mater. **31**(11), 2007447 (2021). https://doi.org/10.1002/adfm.202007447

26. T. Wu, X. Liu, X. Luo, X. Lin, D. Cui et al., Lead-free tin perovskite solar cells. Joule **5**(4), 863–886 (2021). https://doi.org/10.1016/j.joule.2021.03.001

27. M. Chen, Q. Dong, F.T. Eickemeyer, Y. Liu, Z. Dai et al., High-performance lead-free solar cells based on tin-halide perovskite thin films functionalized by a divalent organic cation. ACS Energy Lett. **5**(7), 2223–2230 (2020). https://doi.org/10.1021/acsenergylett.0c00888

28. T. Ye, X. Wang, K. Wang, S. Ma, D. Yang et al., Localized electron density engineering for stabilized B-γ CsSnI$_3$-based perovskite solar cells with efficiencies >10%. ACS Energy Lett. **6**(4), 1480–1489 (2021). https://doi.org/10.1021/acsenergylett.1c00342

29. X. Liu, T. Wu, C. Zhang, Y. Zhang, H. Segawa et al., Interface energy-level management toward efficient tin perovskite solar cells with hole-transport-layer-free structure. Adv. Funct. Mater. **31**(50), 2106560 (2021). https://doi.org/10.1002/adfm.202106560

30. M.A. Kamarudin, D. Hirotani, Z. Wang, K. Hamada, K. Nishimura et al., Suppression of charge carrier recombination in lead-free tin halide perovskite via Lewis base post-treatment. J. Phys. Chem. Lett. **10**(17), 5277–5283 (2019). https://doi.org/10.1021/acs.jpclett.9b02024

31. T. Wang, Q. Tai, X. Guo, J. Cao, C.-K. Liu et al., Highly air-stable tin-based perovskite solar cells through grain-surface protection by gallic acid. ACS Energy Lett. **5**(6), 1741–1749 (2020). https://doi.org/10.1021/acsenergylett.0c00526

32. C. Liu, J. Tu, X. Hu, Z. Huang, X. Meng et al., Enhanced hole transportation for inverted tin-based perovskite solar cells with high performance and stability. Adv. Funct. Mater. **29**(18), 1808059 (2019). https://doi.org/10.1002/adfm.201808059

33. X. Zhang, C. Hägglund, E.M.J. Johansson, Electro-optics of colloidal quantum dot solids for thin-film solar cells. Adv. Funct. Mater. **26**(8), 1253–1260 (2016). https://doi.org/10.1002/adfm.201503338

34. J.-H. Lee, J. Kim, G. Kim, D. Shin, S.Y. Jeong et al., Introducing paired electric dipole layers for efficient and reproducible perovskite solar cells. Energy Environ. Sci. **11**(7), 1742–1751 (2018). https://doi.org/10.1039/C8EE00162F

35. X. Zhang, Z.-K. Yuan, S. Chen, Low electron carrier concentration near the p-n junction interface: A fundamental factor limiting short-circuit current of Cu(In, Ga)S$_e$2 solar cells. Sol. RRL **3**(6), 1900057 (2019). https://doi.org/10.1002/solr.201900057

36. X. Yang, S. Zhang, K. Zhang, J. Liu, C. Qin et al., Coordinated shifts of interfacial energy levels: Insight into electron injection in highly efficient dye-sensitized solar cells. Energy Environ. Sci. **6**(12), 3637–3645 (2013). https://doi.org/10.1039/c3ee42110d

37. S. Zhang, X. Yang, Y. Numata, L. Han, Highly efficient dye-sensitized solar cells: progress and future challenges. Energy Environ. Sci. **6**(5), 1443 (2013). https://doi.org/10.1039/c3ee24453a

38. M.H. Kumar, S. Dharani, W.L. Leong, P.P. Boix, R.R. Prabhakar et al., Lead-free halide perovskite solar cells with high photocurrents realized through vacancy modulation. Adv. Mater. **26**(41), 7122–7127 (2014). https://doi.org/10.1002/adma.201401991

39. K.P. Marshall, M. Walker, R.I. Walton, R.A. Hatton, Enhanced stability and efficiency in hole-transport-layer-free CsSnI$_3$ perovskite photovoltaics. Nat. Energy **1**, 16178 (2016). https://doi.org/10.1038/nenergy.2016.178

40. T. Shi, H.-S. Zhang, W. Meng, Q. Teng, M. Liu et al., Effects of organic cations on the defect physics of tin halide perovskites. J. Mater. Chem. A **5**(29), 15124–15129 (2017). https://doi.org/10.1039/C7TA02662E

41. S.J. Lee, S.S. Shin, J. Im, T.K. Ahn, J.H. Noh et al., Reducing carrier density in formamidinium tin perovskites and its beneficial effects on stability and efficiency of perovskite solar cells. ACS Energy Lett. **3**(1), 46–53 (2018). https://doi.org/10.1021/acsenergylett.7b00976

42. X. Liu, Y. Wang, F. Xie, X. Yang, L. Han, Improving the performance of inverted formamidinium tin iodide perovskite solar cells by reducing the energy-level mismatch. ACS Energy Lett. **3**(5), 1116–1121 (2018). https://doi.org/10.1021/acsenergylett.8b00383

43. X. Liu, Y. Wang, T. Wu, X. He, X. Meng et al., Efficient and stable tin perovskite solar cells enabled by amorphous-polycrystalline structure. Nat. Commun. **11**(1), 2678 (2020). https://doi.org/10.1038/s41467-020-16561-6

44. Y. Bai, S. Xiao, C. Hu, T. Zhang, X. Meng et al., Dimensional engineering of a graded 3D–2D halide perovskite interface enables ultrahigh Voc enhanced stability in the p-i-n photovoltaics. Adv. Energy Mater. **7**(20), 1701038 (2017). https://doi.org/10.1002/aenm.201701038

45. K.T. Cho, S. Paek, G. Grancini, C. Roldan-Carmona, P. Gao et al., Highly efficient perovskite solar cells with a compositionally engineered perovskite/hole transporting material interface. Energy Environ. Sci. **10**(2), 621–627 (2017). https://doi.org/10.1039/c6ee03182j

46. B. Chen, H. Chen, Y. Hou, J. Xu, S. Teale et al., Passivation of the buried interface via preferential crystallization of 2D perovskite on metal oxide transport layers. Adv. Mater. **33**(41), 2103394 (2021). https://doi.org/10.1002/adma.202103394

47. E. Jokar, C.-H. Chien, A. Fathi, M. Rameez, Y.-H. Chang et al., Slow surface passivation and crystal relaxation with additives to improve device performance and durability for tin-based perovskite solar cells. Energy Environ. Sci. **11**(9), 2353–2362 (2018). https://doi.org/10.1039/C8EE00956B

48. T. Wu, X. Liu, X. He, Y. Wang, X. Meng et al., Efficient and stable tin-based perovskite solar cells by introducing

49. π-conjugated lewis base. Sci. China Chem. **63**(1), 107–115 (2020). https://doi.org/10.1007/s11426-019-9653-8

49. T. Wu, D. Cui, X. Liu, X. Luo, H. Su et al., Additive engineering toward high-performance tin perovskite solar cells. Sol. RRL **5**(5), 2100034 (2021). https://doi.org/10.1002/solr.202100034

50. T.M. Koh, T. Krishnamoorthy, N. Yantara, C. Shi, W.L. Leong et al., Formamidinium tin-based perovskite with low E$_g$ for photovoltaic applications. J. Mater. Chem. A **3**(29), 14996–15000 (2015). https://doi.org/10.1039/C5TA00190K

51. Y. Wang, T. Wu, J. Barbaud, W. Kong, D. Cui et al., Stabilizing heterostructures of soft perovskite semiconductors. Science **365**(6454), 687–691 (2019). https://doi.org/10.1126/science.aax8018

52. G. Saianand, P. Sonar, G.J. Wilson, A.-I. Gopalan, V.A.L. Roy et al., Current advancements on charge selective contact interfacial layers and electrodes in flexible hybrid perovskite photovoltaics. J. Energy Chem. **54**, 151–173 (2021). https://doi.org/10.1016/j.jechem.2020.05.050

53. T. Wu, Y. Wang, Z. Dai, D. Cui, T. Wang et al., Efficient and stable CsPbI$_3$ solar cells via regulating lattice distortion with surface organic terminal groups. Adv. Mater. **31**(24), 1900605 (2019). https://doi.org/10.1002/adma.201900605

54. D. Bi, C. Yi, J. Luo, J.-D. Décoppet, F. Zhang et al., Polymer-templated nucleation and crystal growth of perovskite films for solar cells with efficiency greater than 21%. Nat. Energy **1**(10), 16142 (2016). https://doi.org/10.1038/nenergy.2016.142

55. T. Wu, X. Li, Y. Qi, Y. Zhang, L. Han, Defect passivation for perovskite solar cells: from molecule design to device performance. Chemsuschem **14**(20), 4354–4376 (2021). https://doi.org/10.1002/cssc.202101573

56. F. Zhang, J. Song, R. Hu, Y. Xiang, J. He et al., Interfacial passivation of the p-doped hole-transporting layer using general insulating polymers for high-performance inverted perovskite solar cells. Small **14**(19), 1704007 (2018). https://doi.org/10.1002/smll.201704007

57. P. Xu, S. Chen, H.-J. Xiang, X.-G. Gong, S.-H. Wei, Influence of defects and synthesis conditions on the photovoltaic performance of perovskite semiconductor CsSnI$_3$. Chem. Mater. **26**(20), 6068–6072 (2014). https://doi.org/10.1021/cm503122j